An Anti-freezing Pure Inorganic Electrolyte for Long Cycle Life Aqueous Sodium-ion Batteries at -40 °C

Abstract: Aqueous electrolytes have the great application potential for sodium-ion batteries owing to eco-friendliness, high-safety, and low cost. However, the high freezing point of common aqueous electrolytes greatly limits the normal operation of aqueous sodium-ion batteries (ASIBs) at low temperatures. Herein, $MnCl_2·4H_2O$ is introduced into NaCl solution to form the hybrid $NaCl/MnCl_2·4H_2O$ electrolyte to expand the application scope of ASIBs. Due to the strong interaction between Mn^{2+} and water molecules, the hydrogen bond network in water is damaged on a large scale. Thus, the hybrid electrolyte maintains a liquid state and has a high ionic conductivity (2.44 mS cm^{-1}) at -50 °C. When used the optimized hybrid inorganic electrolyte, the pure inorganic compositions full battery assembled with $Na_2CoFe(CN)_6$ cathode and active carbon anode delivers a high specific capacity of 54.0 mAh g^{-1} at -40 °C under 1 C (1 C = 150 mA g^{-1}). Excitingly, when tested at -40 °C under 10 C, the battery can achieve an ultra-long cycle stability of 10,000 cycles with a capacity retention of ~ 99%. Significantly, this work opens a new path to explore the ASIBs with superior electrochemical performance at low temperatures.

Keywords: aqueous sodium-ion batteries, low-temperature, manganese chloride tetrahydrate, pure inorganic electrolyte

1. Introduction

Electrochemical energy storage technologies are of great importance for storage and conversion of the renewable energy sources [1-3]. Recently, sodium-ion batteries (SIBs) attract considerable attention owing to low cost and abundant sodium reserves, which are considered to be a promising alternative to lithium-ion batteries (LIBs), as well as crucial electrical power sources and energy storage systems in future [4-7]. Especially, the most key advantage of SIBs is that the content of sodium 23,000 ppm (2.3%) in Earth's crust is over a thousand times than that of lithium (20 ppm), making it cheap. Benefiting from the similar working principles as LIBs, it has the great potential for mass production for SIBs using the existing technology and manufacturing equipment developed for LIBs [4, 8-12]. As far as large-scale energy storage power stations, safety and cost are the very key factors [13]. It is obvious that the present energy storage systems based on the toxic and flammable organic electrolytes in SIBs field fail to satisfy the green energy demand and raise potential security concerns [14, 15]. By comparison, aqueous electrolytes are expected to be appealing alternatives for commercial organic electrolytes due to the high safety, low cost, eco-friendliness, and so on [13, 14, 16-19]. Nevertheless, the aqueous electrolytes usually deliver the narrow liquid-state temperature range [1]. Owing to the high freezing point of water, the ordinary aqueous electrolyte becomes frozen when the temperature decreases dramatically, which severely limits the migration of ions, resulting in significant loss of capacity [1, 19-21]. Even for the advanced commercial batteries, capacity and rate performance degrade rapidly at temperatures below 0 °C and completely fail below -20 °C [22-24]. Some activities such as high venturing, polar expeditions, outdoor adventures, and military campaigns require a sustainable and efficient power source at extremely low temperatures. Yet, the inherent shortcoming of aqueous electrolytes of being frozen dramatically reduces their low-temperature adaptation, resulting in an unavailability for human activities [25]. As a consequence, the development of novel aqueous electrolytes that remain unfrozen is urgent for enhancing the electrochemical performance and expanding the application requirements of ASIBs in subzero environment.

Great efforts have been made for improving the performance of ASIBs under below-zero temperatures, and some groundbreaking studies have been conducted to lower the freezing point of aqueous electrolytes by adding organic solutions as co-solvents, such as formamide [17], methanol [26], sulfolane (SL) [27], acetonitrile [28, 29], dimethyl sulfoxide [19], and ethylene glycol [30], all of them can effectively reduce the freezing point of aqueous electrolytes. However, these organic solvents usually lead to an increase of electrolyte viscosity and a decrease of dielectric constant, which severely reduces ionic conductivity. Furthermore, expensive and volatile organic additives hinder the safe and environmentally friendly development of energy storage systems. An effective design strategy was proposed to use high concentration electrolytes to lower their freezing point [1, 31]. For instance, Chen *et al.* reported that the 7.5 m $ZnCl_2$ electrolyte possesses an ionic conductivity of 1.79 mS cm^{-1} at -60 °C [1]. Zhang *et al.* used 17 m $NaClO_4$ electrolyte to obtain SIBs with a long lifespan at -30 °C (98% capacity retention over 1000 cycles) [31]. However, the very high concentration of electrolyte leads to high viscosity at low temperatures and high cost, which are unfavorable for ion migration and large-scale applications [16]. Therefore, the low-concentration pure inorganic aqueous electrolytes with endurance at low temperatures are in great demand.

For the first time, $MnCl_2 \cdot 4H_2O$ was introduced into NaCl solution to lower the freezing point of aqueous electrolytes for ASIBs in this work. A low-concentration anti-freezing electrolyte containing NaCl and $MnCl_2 \cdot 4H_2O$ was designed for ASIBs. The $NaCl/MnCl_2 \cdot 4H_2O$ hybrid electrolyte, benefiting from the strong interaction between Mn^{2+} and water molecules, the original hydrogen bond network between water molecules is disrupted on a large scale, realizing an ultra-low freezing point, which is much lower than that of the conventional NaCl electrolyte (Fig. 1). As expected, the hybrid electrolyte still maintains an unfreezing state and has a high ionic conductivity at -50 °C. The ASIBs using $NaCl/MnCl_2 \cdot 4H_2O$ aqueous electrolyte can be operated at -40 °C and keep excellent capacity retention at extremely cold temperatures. This work is expected to broaden the design concepts of freezing-resistant electrolytes and promote the aqueous batteries application for the large-scale energy storage with wide operating temperatures range.

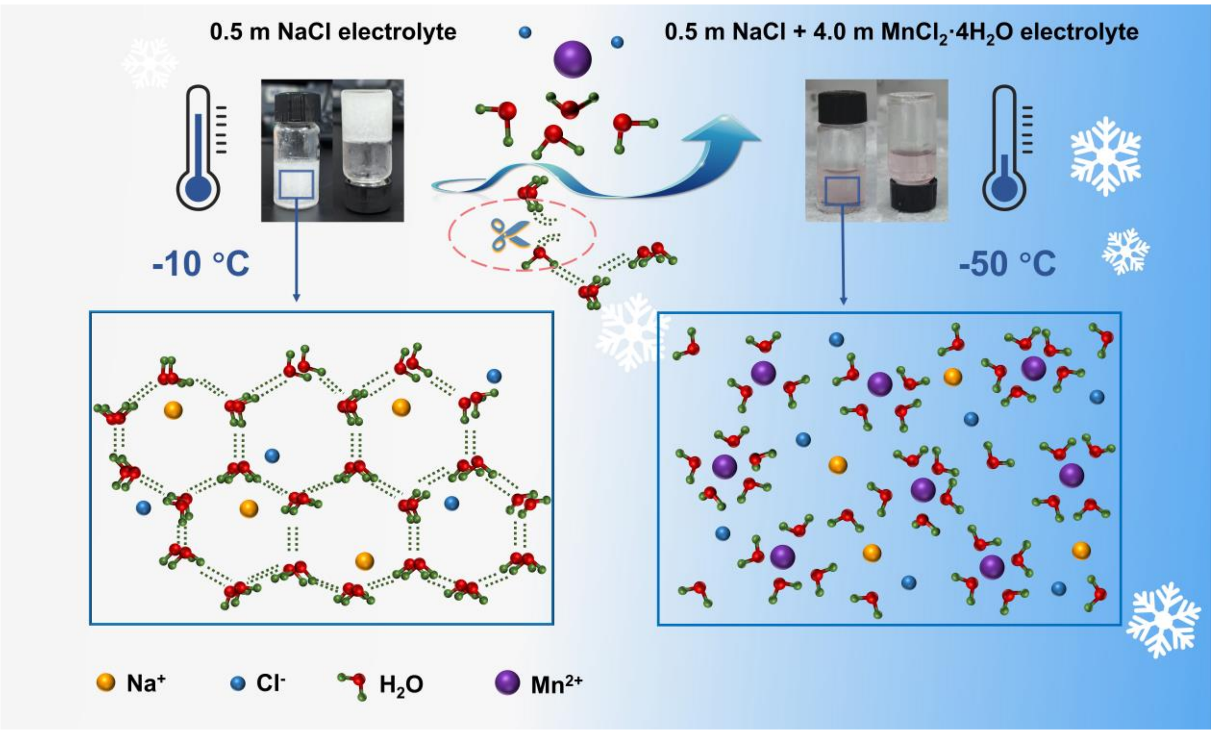

Fig. 1. Schematic diagram and the anti-freezing mechanism for the pure inorganic electrolyte.

2. Results and Discussion

In this work, both the electrodes and the electrolyte are made of pure inorganic materials, as can be clearly shown in Fig. 2a. As we all know, the freezing point and conductivity of the electrolyte are two very key factors for the low-temperature performance of aqueous batteries [13, 17, 22, 32]. Generally, the viscosity of the electrolyte increases with the decrease of temperature, which leads to a decrease of the ion transport rate [22]. As the environmental temperature approaches the freezing point of the electrolyte, the viscosity increases rapidly, which makes it difficult for the ions to migrate efficiently [13]. The conductivity of electrolytes at low temperatures is usually much lower than that of room temperature, which is the reason for unsatisfactory performance or even failure of the battery at low temperatures [22-24].

Therefore, reducing the freezing point of the electrolyte and increasing its conductivity are very effective methods to achieve high-performance battery at low temperatures. The optimized electrolyte is composed of 0.5 m (mol·L^{-1}) NaCl and a certain concentration of $MnCl_2·4H_2O$. In order to accurately determine the appropriate $MnCl_2·4H_2O$ concentration ($C_{MnCl_2·4H_2O}$), a series of solution samples with different concentrations were placed under different temperatures for 2 hours, as demonstrated in Fig. 2b. The prepared samples are expressed as 0.5 m NaCl + ξ m $MnCl_2·4H_2O$ (ξ = 0, 0.5, 1.0, 1.5, 2.0, 2.5, 3.0, 3.5, 4.0, 4.5). All of the samples appear completely transparent and unfrozen at room temperature (25 °C). When the environmental temperature reaches -30 °C, the samples with $C_{MnCl_2·4H_2O} \leq 2.0$ m exhibit an opaque and completely frozen state. As the temperature continues to drop to -60 °C, only solution with $C_{MnCl_2·4H_2O} = 4.0$ m remains transparent and unfrozen, while the other samples appear completely frozen, indicating that the optimized mixed solution 0.5 m NaCl + 4.0 m $MnCl_2·4H_2O$ has the lowest freezing point among all the samples. For clear comparison, the optical photographs of all the samples at different temperatures (0 °C, -10 °C, -20 °C, -40 °C, -50 °C) are shown in Fig. S1. The samples gradually freeze with decreasing of temperature, and the lower-concentration samples freeze earlier than the higher-concentration samples, for instance, the sample with $C_{MnCl_2·4H_2O} = 0.5$ m becomes frozen state at -20 °C, whereas the sample with $C_{MnCl_2·4H_2O} = 2.0$ m gets frozen at -40 °C, indicating that the freezing resistance of the solution enhances with increasing of concentration. It should be noted that the salt precipitation can be clearly observed at -40 °C for the solution with $C_{MnCl_2·4H_2O} = 4.5$ m, which becomes completely frozen at

-60 °C (Fig. S1d and Fig. 2b). This is due to the fact that the concentration of the solution is close to saturation and solubility decreases drastically with decreasing temperature leading to salt precipitation; at the same time, the concentration of the solution exceeds the eutectic concentration, thus the freezing point will not continue to decrease [16, 25]. To further verify the stability freezing point for different electrolytes, the states of 0.5 m NaCl electrolyte and the optimized 0.5 m NaCl + 4.0 m $MnCl_2 \cdot 4H_2O$ electrolyte were observed at low temperatures (below -5 °C) for 24 h, respectively. For 0.5 m NaCl electrolyte, the ice crystal can be clearly found at -5 °C (Fig. S2) and completely freeze at -10 °C (Fig. S3). Compared with 0.5 m NaCl electrolyte, the optimized electrolyte (0.5 m NaCl + 4.0 m $MnCl_2 \cdot 4H_2O$) remains a transparent state and has good fluidity after being placed at -50 °C (Fig. S4). The above results suggest that the freezing resistance of the 0.5 m NaCl electrolyte is greatly improved with the addition of 4.0 m $MnCl_2 \cdot 4H_2O$.

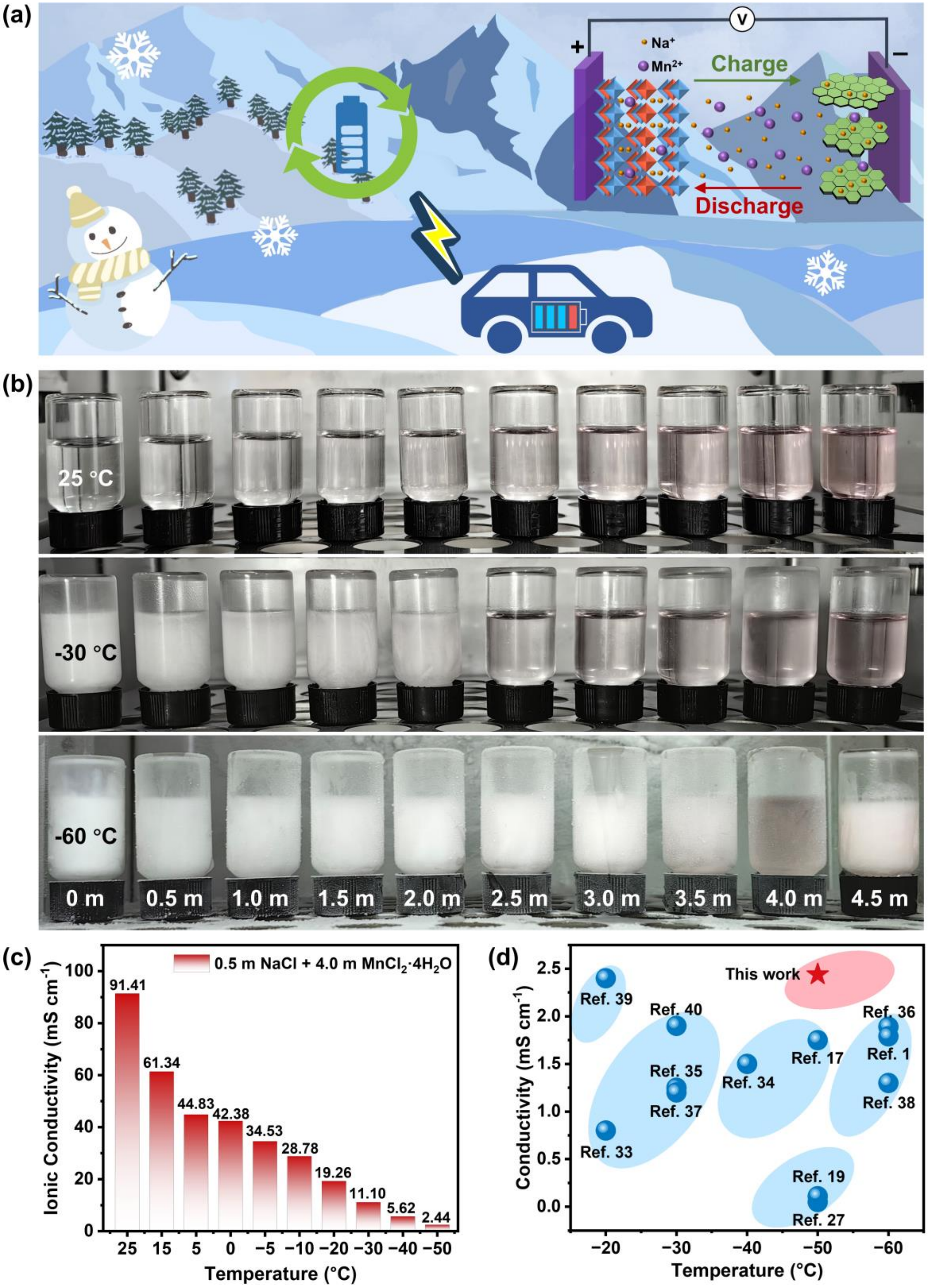

Fig. 2. (a) The operating schematic diagram of the pure inorganic storage system in this work. (b) The optical images of 0.5 m NaCl-based solutions with different concentrations of $MnCl_2·4H_2O$ under 25 ℃, -30 ℃ and -60 ℃. (c) The ionic conductivity of 0.5 m NaCl + 4.0 m $MnCl_2·4H_2O$ electrolyte at different temperatures. (d) The comparison of conductivity between this work and previous reports at different temperatures.

The conductivity of electrolytes can be calculated from the electrochemical impedance spectra (EIS) measurements. The EIS results of 0.5 m NaCl and 0.5 m NaCl + 4.0 m $MnCl_2·4H_2O$ electrolyte at different temperatures are displayed in Figs. S5a and b, respectively. At room temperature (25 °C), the conductivity of 0.5 m NaCl + 4.0 m $MnCl_2·4H_2O$ electrolyte (Fig. 2c) is 91.41 mS cm^{-1}, which is almost 2 times higher than that of the 0.5 m NaCl electrolyte (46.62 mS cm^{-1}, Fig. S6). Even at -50 °C, the conductivity of 0.5 m NaCl + 4.0 m $MnCl_2·4H_2O$ electrolyte reaches a satisfactory 2.44 mS cm^{-1}, which is much higher than the reported results shown in Fig. 2d [1, 17, 19, 27, 33-40]. In particular, it is more than 48 times that of the $LiClO_4$ electrolyte with SL addition (0.05 mS cm^{-1}) [27]. Therefore, it is expected that the optimized 0.5 m NaCl + 4.0 m $MnCl_2·4H_2O$ electrolyte is an ideal electrolyte material for low-temperature aqueous batteries.

The illogical high freezing point of pure water is caused by the abundant hydrogen bonds in water [1]. Hence, the freezing point of water can be lowered by breaking the hydrogen bond network between water molecules. It is well known that the electrostatic interactions between metal ions and polar water molecules are very strong, and thereby the hydrogen bond network can be disrupted by the introduction of metal ions [1, 41, 42]. In order to theoretically reveal the effect of $MnCl_2·4H_2O$ on lowering the freezing point of 0.5 m NaCl electrolyte, density functional theory (DFT) has been carried out to calculate the interaction energy ($E_{\text{interaction}}$) between individual particle for 0.5 m NaCl + 4.0 m $MnCl_2·4H_2O$ electrolyte. As shown in Fig. 3a, it can be clearly observed that the $E_{\text{interaction}}$ of Mn^{2+}-H_2O (-65.93 kJ mol^{-1}) is far lower than those other energies, suggesting that water molecules prefer to interact with Mn^{2+} rather than other water molecules. The hydrogen bonding in the water molecules have been broken drastically. Molecular dynamics (MD) simulations have been performed to obtain the overall interaction energies among particles in the electrolyte, together with the evolution of hydrogen bond network for different electrolytes. As displayed in Fig. S7, the overall $E_{\mathrm{interaction}}$ among all the water molecules is -146.62×10^3 kJ mol^{-1} for 0.5 m NaCl + 4.0 m $MnCl_2 \cdot 4H_2O$ electrolyte, which is much higher than that of 0.5 m NaCl electrolyte system (-206.97×10^3 kJ mol^{-1}), revealing the weak bonding between water molecules in the mixture electrolyte [43]. The MD simulation snapshots in Fig. 3b show that after the addition of 4.0 m $MnCl_2 \cdot 4H_2O$ into 0.5 m NaCl electrolyte, the hydrogen bonds between water molecules are markedly reduced compared with 0.5 m NaCl electrolyte, and a large number of $Mn^{2+} \cdots O\text{-}H$ bonds are formed, well consistent with the DFT results shown in Fig. 3a. The reduction of the number of free water molecules in the mixed electrolyte can remarkably enhance the freezing tolerance for the mixed electrolyte [43]. Statistical analysis shows that, in Fig. 3c, the average number of hydrogen bonds between water molecules is 1.065 in the optimized 0.5 m NaCl + 4.0 m $MnCl_2 \cdot 4H_2O$ electrolyte, far lower than 1.618 in 0.5 m NaCl electrolyte, indicating a significant reduction of the number of hydrogen bonds, which can be attributed to the strong interaction between Mn^{2+} and water molecules as confirmed by DFT results in Fig. 3a. Thus, the optimized pure inorganic electrolyte 0.5 m NaCl + 4.0 m $MnCl_2 \cdot 4H_2O$ is expected to be a promising candidate for the ASIBs.

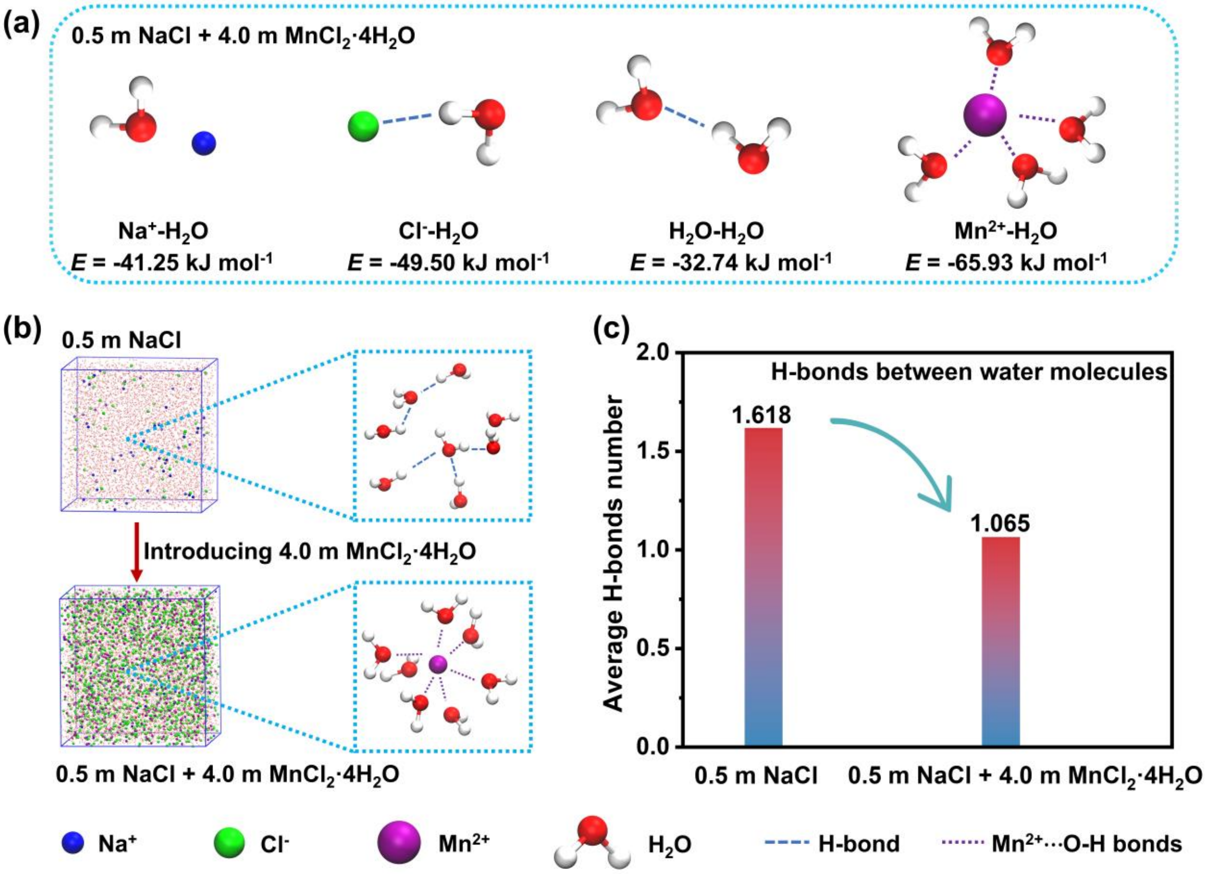

Fig. 3. (a) The interaction energy from DFT calculation for individual H_2O molecule and other particle in 0.5 m NaCl + 4.0 m $MnCl_2·4H_2O$ electrolyte. (b) MD simulation snapshots for 0.5 m NaCl (upper) and 0.5 m NaCl + 4.0 m $MnCl_2·4H_2O$ (lower) electrolyte, respectively. (c) The average number of hydrogen bonds between water molecules for different electrolytes.

The anti-freezing mechanism of $MnCl_2·4H_2O$ solution can be further elaborated by Raman spectra. Fig. 4a shows the Raman spectra of pure water and 0.5 m NaCl + ξ m $MnCl_2·4H_2O$ (ξ = 0, 2.0, 4.0) electrolytes. For pure water, the broad Raman peak locating within 3000-3700 cm^{-1} relates to the O-H stretching vibration, which is usually divided into three components. The main peaks at around 3230 cm^{-1}, 3450 cm^{-1}, and 3620 cm^{-1} correspond to the strong hydrogen bond water (SHW), the weak hydrogen bond water (WHW), and non-hydrogen bond water (NHW), respectively [1, 16, 25].

For SHW, four hydrogen bonds are usually formed around one water molecule. With respect to NHW, no hydrogen bond exists around water molecules. As to WHW, the number of hydrogen bonds around one water molecule lies between that of SHW and NHW [16]. In terms of liquid water, the water molecules are in natural vibration, and the hydrogen bonds between water molecules are in a state of constant formation and fracture [13]. The essence of water crystallization is the transformation of randomly dispersed water molecules into an ordered ice state under the influence of hydrogen bonds [32]. Thus, the freezing point of solutions can be significantly lowered by breaking the hydrogen bond network of water (reducing the content of SHW) [16]. As depicted in Fig. 4a, the existence of a notable shoulder peak at ~ 3230 cm^{-1} means a marked amount of SHW in pure water. Compared with that of pure water, the shoulder peak at ~ 3230 cm^{-1} for 0.5 m NaCl solution keeps almost unchanged, indicating the negligible influence of NaCl solution on SHW content. With increasing of $MnCl_2 \cdot 4H_2O$ concentration, the intensity of shoulder peak at ~ 3230 cm^{-1} significantly weakens and the peak value gradually moves to higher wavenumber, indicating a decrease of SHW content [13]. In order to quantify the proportion of the water with the different hydrogen-bound states, the ratios are calculated on the basis of the areas of the fitted peaks in Figs. 4b-d and Fig. S8 [1, 16]. The results in Fig. 4e show that, the SHW content is 48.1%, 46.9%, 36.4%, and 26.7%, and the content of WHW is 44.9%, 45.7%, 62.6%, and 69.7% for pure water, 0.5 m NaCl, 0.5 m NaCl + 2.0 m $MnCl_2 \cdot 4H_2O$, and 0.5 m NaCl + 4.0 m $MnCl_2 \cdot 4H_2O$ electrolyte, respectively. The SHW rapidly reduces while WHW significantly increases with the increase of $MnCl_2 \cdot 4H_2O$ concentration, indicating the progressive destruction of hydrogen bond network structure. It should be noted that the content of SHW shows the lowest value under $C_{MnCl_2 \cdot 4H_2O}$ = 4.0 m, meaning the most decline in the freezing point, in good consistent with the results shown in Fig. 2b and MD simulations in Fig. 3.

The Fourier transform infrared (FTIR) spectra in Fig. 4f show the main peak at 2800-3600 cm^{-1}, corresponding to the vibration of O-H, shifts to higher wavenumber with increasing of $MnCl_2 \cdot 4H_2O$ concentration, revealing the weakening of hydrogen bonds between water molecules [44, 45]. This can be ascribed to the disruption of the hydrogen bond network structure caused by the addition of Mn^{2+}, in good agreement with the results of Raman tests and MD simulations.

The differential scanning calorimetry (DSC) measurements were measured for 0.5 m NaCl + ξ m $MnCl_2 \cdot 4H_2O$ (ξ = 0, 1.0, 2.5, 4.0) electrolytes to elaborate the effect of $MnCl_2 \cdot 4H_2O$ on the freezing point of NaCl solution, as shown in Fig. 4g and Fig. S9. Normally, a sharp endothermic peak arises during the ice-melting process, and a distinct step appears during the glass transition process [1, 43]. During the heat-absorbing process (from -80 °C to 25 °C), a distinct sharp endothermic peak can be observed in the case of the $C_{MnCl_2 \cdot 4H_2O}$ < 4.0 m (Fig. S9), while, the endothermic peak disappears under $C_{MnCl_2 \cdot 4H_2O}$ = 4.0 m. DSC curve from 25 °C to -150 °C is displayed in Fig. 4g. According to the references [46-48], the onset and the width of the glass transition (T_g) of the hybrid electrolyte with $C_{MnCl_2 \cdot 4H_2O}$ = 4.0 m are -106 °C and -106 ~ -116 °C, respectively. As a result, the 4.0 m $MnCl_2 \cdot 4H_2O$ is expected to be an ideal material to lower the freezing point and improve the freezing resistance of the 0.5 m NaCl electrolyte. Figure 4h presents linear sweep voltammetry curves (LSV) for different solutions. It can be seen that electrochemical stability window (ESW) of the optimized 0.5 m NaCl + 4.0 m $MnCl_2 \cdot 4H_2O$, 0.5 m NaCl and pure 4.0 m $MnCl_2 \cdot 4H_2O$ solution is ~ 2.28, 2.4 and 2.02 V, much higher than the theoretical decomposition voltage of water (~ 1.23 V) [17, 49, 50], as well as higher than that of the conventional aqueous electrolytes (≤ 2V) [50]. Hence, the optimized electrolyte has great advantages for electrochemical working in practical applications.

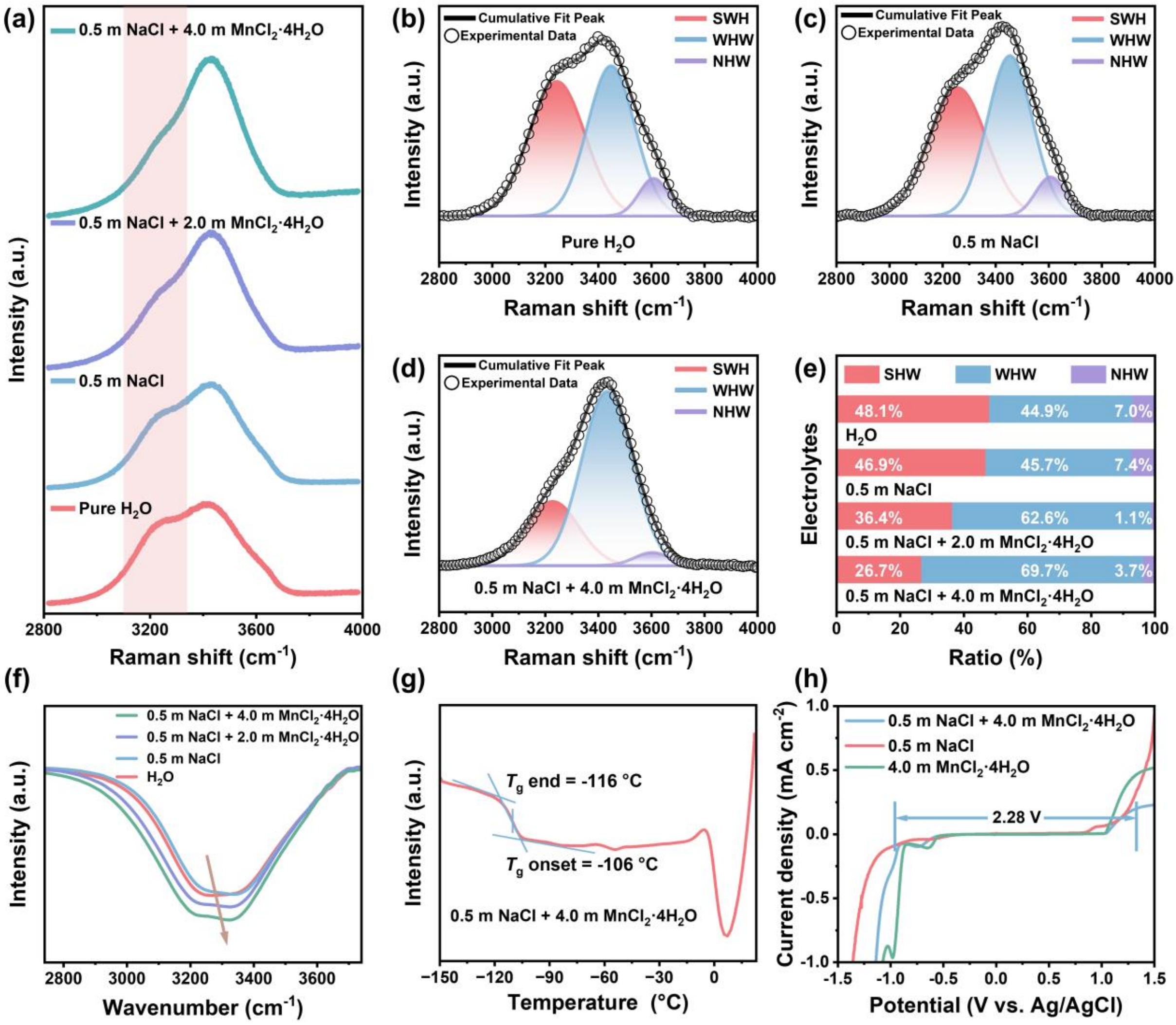

Fig. 4. (a) Raman spectra of pure water and NaCl-based electrolytes. (b)-(d) The correspondingly fitted O-H stretching vibrations based on Fig. 4(a) for pure water, 0.5 m NaCl electrolyte, 0.5 m NaCl + 4.0 m $MnCl_2{\cdot}4H_2O$ electrolyte, respectively. (e) The ratios of water with different hydrogen-bound states for various electrolytes (f) FTIR results for various electrolytes. (g) DSC curve of 0.5 m NaCl + 4.0 m $MnCl_2{\cdot}4H_2O$ electrolyte. (h) LSV curves for different solutions.

To evaluate the practical applications of the optimized electrolyte, ASIBs were constructed with $Na_2CoFe(CN)_6$, active carbon (AC), and the optimized 0.5 m NaCl + 4.0 m $MnCl_2{\cdot}4H_2O$ electrolyte as cathode, anode, and electrolyte, respectively. The morphological and structural characterizations for the electrode materials are shown in Figs. S10-S12. The electrochemical performance of $Na_2CoFe(CN)_6$ electrode was measured by cyclic voltammetry (CV) in the optimized 0.5 m NaCl + 4.0 m $MnCl_2 \cdot 4H_2O$ electrolyte. As displayed in Fig. S13, the CV curves of $Na_2CoFe(CN)_6$ electrode show reversible redox peaks, and all CV curves almost completely overlap in 3 cycles, demonstrating excellent stability and good compatibility with the electrolyte [51]. The ASIBs were charged and discharged at a current density of 1 C (1 C = 150 mA g^{-1}) under different temperatures and the specific capacities are 101.8, 82.7, 78.9, 72.4, 65.5, and 55.9 mAh g^{-1} at 25, 0, -10, -20, -30, and -40 °C, respectively (Figs. 5a and S14a). Compared with the specific capacity at 25 °C, the capacity retention of the ASIBs is 54.9% at -40 °C. When the temperature rises from -40 °C to 25 °C, the specific capacity of ASIBs can nearly restore to the initial level, indicating that the freeze-resistant performance of ASIBs is highly reversible. Fig. 5b shows the cycling tests of ASIBs measured at -40 °C after 10 activation cycles. The specific capacity of ASIBs at -40 °C is up to 54.0 mAh g^{-1} at 1 C, and even after 1000 cycles, the battery maintains a specific capacity of 51.0 mAh g^{-1} at 1 C, with 94.4% of the capacity retention to the initial cycle. The negligible capacity attenuation during long-term operation in harsh cold environments indicates that ASIBs own excellent electrochemical properties and can meet the application requirements of energy storage power stations in the extreme cold regions. Furthermore, as confirmed by Fig. 2d, the optimized electrolyte delivers high ionic conductivity at ultra-low temperatures, thus, the freezing-resistant ASIBs possess a good rate performance at low temperatures. When the current density is increased from 1 C to 10 C at -40 °C, the specific capacity still reaches 28.0 mAh g^{-1}, 48% of the specific capacity at 1 C, as shown in Fig. 5c and Fig. S14b. Importantly, when the current density converts back to 1 C from 10 C, the specific capacity also correspondingly restores to the initial specific capacity of 1 C, revealing that ASIBs deliver excellent rate capability under ultra-low temperatures. In addition, the freeze-resistant ASIBs exhibit excellent long-term cycling stability, with capacity retention of ~ 100% after 4000 cycles at 5 C under -40 °C (Fig. S15), and ~ 99% after 10,000 cycles at a higher current density of 10 C (Fig. 5d), which is outperforming the previously reported results (Fig. 5e) [27, 29, 33, 35, 36, 39, 41, 43, 52-58].

In order to assess the extremely low-temperature application of the energy storage system, two series connected ASIBs can light three LED bulbs connected in parallel (rated power of 0.02 W, excitation voltage of 1.8 V) at -50 °C (Fig. 5f and Video S1), which is much lower than most of the human activity temperature ranges. Even stored at -50 ℃ for a month, two series ASIBs can still power the three parallel LED bulbs (rated power of 0.02 W, excitation voltage of 1.8 V) when the circuit is turned on (Fig. S16), demonstrating the excellent stability of the system in ultra-low temperatures. As expected, this freezing-resistant ASIBs energy storage system presents the excellent ultra-low-temperature performance and practical application prospect.

Owing to the coexistence of Mn^{2+} and Na^{+} in the optimized electrolyte, it is necessary to verify the real identity of the carrier ions during the cycling process. The $Na_2CoFe(CN)_6$ electrode was first charged and discharged several times in the potential range of 0 ~1 V using 0.5 m NaCl + 4.0 m $MnCl_2 \cdot 4H_2O$ as electrolyte (Ag/AgCl and AC were used as the reference electrode and the counter electrode, respectively). Then, the ex-situ XPS tests were performed for $Na_2CoFe(CN)_6$ electrode when charged to 1

V and discharged to 0 V, respectively. As shown in Fig. S17, when measured at 1 V, a weak peak of Na 1s at ~ 1071.5 eV is detected, which is attributed to the continuous release of Na^+ from the positive electrode during charging. When the XPS test was performed at 0 V, a strong peak of Na 1s can be observed at ~ 1070.8 eV, which is because of the constant embedding of Na^+ into the positive electrode during the discharging. However, the strong peaks of Mn 2p locating at ~ 641.0 eV and 653.1 eV can be detected regardless of the potential of 1 V or 0 V, indicating that part of Mn^{2+} embeds into the $Na_2CoFe(CN)_6$ electrode during the charging and discharging. To preliminarily investigate the effect of Mn^{2+} in $Na_2CoFe(CN)_6$ electrode on the capacity of freezing-resistant ASIBs, charge-discharge cycling tests were performed for the $Na_2CoFe(CN)_6$ electrode using 0.5 m NaCl, 4.0 m $MnCl_2 \cdot 4H_2O$, and 0.5 m NaCl + 4.0 m $MnCl_2 \cdot 4H_2O$ electrolytes, respectively. The obtained specific capacities (in Fig. S18) in the three electrolytes are 105 mAh g^{-1}, 38 mAh g^{-1}, and 100 mAh g^{-1}, respectively, indicating the slight influence of Mn^{2+} on the capacity of freeze-resistant ASIBs (~ 5% reduction), which is acceptable. Especially, as depicted in Figs. S18a-c, the 10th, 20th, and 30th charge/discharge curves of $Na_2CoFe(CN)_6$ electrode in the optimized 0.5 m NaCl + 4.0 m $MnCl_2 \cdot 4H_2O$ electrolyte are almost entirely overlapped, verifying that the $Na_2CoFe(CN)_6$ electrode has good stability in the optimized electrolyte, good agreement with the CV results shown in Fig. S13c.

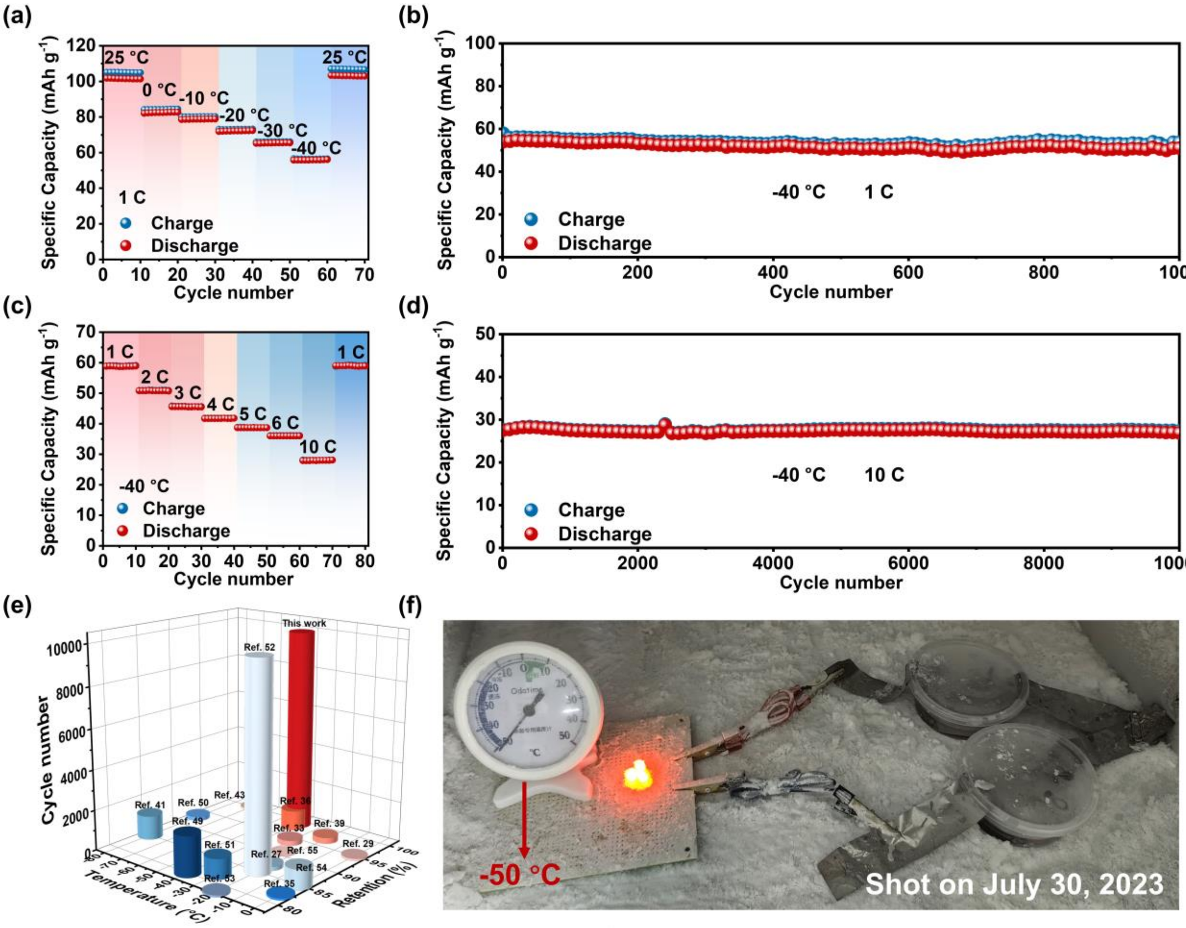

Fig. 5. The electrochemical performance of $Na_2CoFe(CN)_6$//AC full battery using 0.5 m NaCl + 4.0 m $MnCl_2·4H_2O$ electrolyte. (a) The specific capacity of full battery at 1 C in the temperature range of 25 °C to -40 °C. (b) Cyclic performances of the full battery at 1 C under -40 °C. (c) Rate performance at a low temperature of -40 °C. (d) Long cycle life test at a rate of 10 C under -40 °C. (e) Comparison of cycling stability of battery in this work and previous reports at low temperatures. (f) The optical image of the working battery at -50 °C.

3. Conclusion

In summary, the novel pure inorganic NaCl/$MnCl_2·4H_2O$ hybrid electrolyte is developed for ultra-low temperature ASIBs. On the basis of the optical images and DSC results, the optimized pure inorganic electrolyte has an ultra-low freezing point (< -50 °C). The anti-freezing mechanism originates from the significantly destroyed hydrogen bond network between water molecules caused by the addition of Mn^{2+}. At -50 °C, the optimized pure inorganic electrolyte 0.5 m NaCl + 4.0 m $MnCl_2·4H_2O$ owns a wider ESW (~ 2.28 V) and the desired ionic conductivity (2.44 mS cm^{-1}). With these merits, the assembled full batteries based on $Na_2CoFe(CN)_6$//AC deliver excellent ultralow temperature performance at -40 °C, such as 54.9% capacity retention compared to that of room temperature and ~ 99% capacity retention after 10,000 cycles at 10 C. To our huge relief, even after being stayed at -50 °C for a month, the assembled freeze-resistant ASIBs can light up the LED bulbs, demonstrating the extraordinary stability in extreme environments. Encouraged by this, our work will significantly widen the application scenarios and open a new route for the development of low-temperature rechargeable aqueous batteries.

Acknowledgements

This work was financially supported by the National Natural Science Foundation of China (Grant No. 62374107), Shanghai Local Universities Capacity Building Project of Science and Technology Innovation Action Program (21010501700), Class III Peak Discipline of Shanghai-Materials Science and Engineering (High-Energy Beam Intelligent Processing and Green Manufacturing), Open project of Key Laboratory of Artificial Structures and Quantum Control (Ministry of Education), Engineering and Physical Sciences Research Council (EPSRC, EP/V027433/3), EPSRC Centre for Doctoral Training in Molecular Modelling and Materials Science (EP/L015862/1), UK Research and Innovation (UKRI) under the UK government's Horizon Europe funding (101077226; EP/Y008707/1).

Supplementary materials

Supplementary material associated with this article can be found, in the online version or from the authors.

References

[1] Q. Zhang, Y. Ma, Y. Lu, L. Li, F. Wan, K. Zhang, J. Chen, Modulating electrolyte structure for ultralow temperature aqueous zinc batteries, Nat. Commun. 11 (2020) 4463. https://doi.org/10.1038/s41467-020-18284-0

[2] Y. Yamada, J. Wang, S. Ko, E. Watanabe, A. Yamada, Advances and issues in developing salt-concentrated battery electrolytes, Nat. Energy 4 (2019) 269-280. https://doi.org/10.1038/s41560-019-0336-z

[3] Y. Lu, L. Li, Q. Zhang, Z. Niu, J. Chen, Electrolyte and Interface Engineering for Solid-State Sodium Batteries, Joule 2 (2018) 1747-1770. https://doi.org/10.1016/j.joule.2018.07.028

[4] Y. Jin, P. M. L. Le, P. Gao, Y. Xu, B. Xiao, M. H. Engelhard, X. Cao, T. D. Vo, J. Hu, L. Zhong, B. E. Matthews, R. Yi, C. Wang, X. Li, J. Liu, J. Zhang, Low-solvation electrolytes for high-voltage sodium-ion batteries, Nat. Energy 7 (2022) 718-725. https://doi.org/10.1038/s41560-022-01055-0

[5] C. Yang, S. Xin, L. Mai, Y. You, Materials Design for High-Safety Sodium-Ion Battery, Adv. Energy Mater. 11 (2021) 2000974. https://doi.org/10.1002/aenm.202000974

[6] K. Kaliyappan, T. Or, Y. P. Deng, Y. Hu, Z. Bai, Z. Chen, Constructing Safe and Durable High-Voltage P2 Layered Cathodes for Sodium Ion Batteries Enabled by Molecular Layer Deposition of Alucone, Adv. Funct. Mater. 30 (2020) 1910251. https://doi.org/10.1002/adfm.201910251

[7] W. Zhong, M. Tao, W. Tang, W. Gao, T. Yang, Y. Zhang, R. Zhan, S. J. Bao, M. Xu, MXene-derivative pompon-like $Na_2Ti_3O_7$@C anode material for advanced sodium ion batteries, Chem. Eng. J. 378 (2019) 122209. https://doi.org/10.1016/j.cej.2019.122209

[8] Y. Zhao, Y. Kang, J. Wozny, J. Lu, H. Du, C. Li, T. Li, F. Kang, N. Tavajohi, B. Li, Recycling of sodium-ion batteries, Nat. Rev. Mater. 8 (2023) 623-634. https://doi.org/10.1038/s41578-023-00574-w

[9] Y. Li, F. Wu, Y. Li, M. Liu, X. Feng, Y. Bai, C. Wu, Ether-based electrolytes for sodium ion batteries, Chem. Soc. Rev. 51 (2022) 4484-4536. https://doi.org/10.1039/d1cs00948f

[10] A. Joshi, S. Chakrabarty, S. H. Akella, A. Saha, A. Mukherjee, B. Schmerling, M. Ejgenberg, R. Sharma, M. Noked, High-Entropy Co-Free O3-Type Layered Oxyfluoride: A Promising Air-Stable Cathode for Sodium-Ion Batteries, Adv. Mater. 35 (2023) 2304440. https://doi.org/10.1002/adma.202304440

[11] K. Wang, H. Zhuo, J. Wang, F. Poon, X. Sun, B. Xiao, Recent Advances in Mn-Rich Layered Materials for Sodium-Ion Batteries, Adv. Funct. Mater. 33 (2023) 2212607. https://doi.org/10.1002/adfm.202212607

[12] W. Wang, Y. Gang, Z. Hu, Z. Yan, W. Li, Y. Li, Q. F. Gu, Z. Wang, S. L. Chou, H. K. Liu, S. X. Dou, Reversible structural evolution of sodium-rich rhombohedral Prussian blue for sodium-ion batteries, Nat. Commun. 11 (2020) 980. https://doi.org/10.1038/s41467-020-14444-4

[13] K. Zhu, Z. Li, Z. Sun, P. Liu, T. Jin, X. Chen, H. Li, W. Lu, L. Jiao, Inorganic Electrolyte for Low-Temperature Aqueous Sodium Ion Batteries, Small 18 (2022) 2107662. https://doi.org/10.1002/smll.202107662

[14] M. Liu, H. Ao, Y. Jin, Z. Hou, X. Zhang, Y. Zhu, Y. Qian, Aqueous rechargeable sodium ion batteries: developments and prospects, Mater. Today Energy 17 (2020) 100432. https://doi.org/10.1016/j.mtener.2020.100432

[15] T. Liang, R. Hou, Q. Dou, H. Zhang, X. Yan, The Applications of Water-in-Salt Electrolytes in Electrochemical Energy Storage Devices, Adv. Funct. Mater. 31 (2021) 2006749. https://doi.org/10.1002/adfm.202006749

[16] C. You, W. Wu, W. Yuan, P. Han, Q. Zhang, X. Chen, X. Yuan, L. Liu, J. Ye, L. Fu, Y. Wu, Brine Refrigerants for Low-cost, Safe Aqueous Supercapacitors with Ultra-long Stable Operation at Low Temperatures, Adv. Funct. Mater. 33 (2023) 2208206. https://doi.org/10.1002/adfm.202208206

[17] K. Zhu, Z. Sun, Z. Li, P. Liu, X. Chen, L. Jiao, Aqueous sodium ion hybrid batteries with ultra-long cycle life at -50 °C, Energy Storage Mater. 53 (2022) 523-531. https://doi.org/10.1016/j.ensm.2022.09.019

[18] B. Xiang, J. Zhang, X. Zhang, W. Yan, J. Xu, J. Wang, H. Yu, L. Yan, L. Zhang, J. Shu, Common ion effect enhanced cobalt hexacyanoferrate for aqueous Na-ion battery, Composites, Part B 246 (2022) 110241. https://doi.org/10.1016/j.compositesb.2022.110241

[19] Q. Nian, J. Wang, S. Liu, T. Sun, S. Zheng, Y. Zhang, Z. Tao, J. Chen, Aqueous Batteries Operated at -50 °C, Angew. Chem., Int. Ed. 58 (2019) 16994-16999. https://doi.org/10.1002/anie.201908913

[20] X. Gao, J. Yang, Z. Xu, Y. Nuli, J. Wang, Recent progress of aqueous and organic/aqueous hybrid electrolytes for low-temperature rechargeable metal-ion batteries and supercapacitors, Energy Storage Mater. 54 (2023) 382-402. https://doi.org/10.1016/j.ensm.2022.10.046

[21] H. Bai, X. Zhu, H. Ao, G. He, H. Xiao, Y. Chen, Advances in sodium-ion batteries at low-temperature: Challenges and strategies, J. Energy Chem. 90 (2024) 518-539. https://doi.org/10.1016/j.jechem.2023.11.004

[22] R. Hou, S. Guo, H. Zhou, Atomic Insights into Advances and Issues in Low-Temperature Electrolytes, Adv. Energy Mater. 13 (2023) 2300053. https://doi.org/10.1002/aenm.202300053

[23] H. Wang, Z. Chen, Z. Ji, P. Wang, J. Wang, W. Ling, Y. Huang, Temperature adaptability issue of aqueous rechargeable batteries, Mater. Today Energy 19 (2021) 100577. https://doi.org/10.1016/j.mtener.2020.100577

[24] L. Yan, J. Huang, Z. Guo, X. Dong, Z. Wang, Y. Wang, Solid-State Proton Battery Operated at Ultralow Temperature, ACS Energy Lett. 5 (2020) 685-691. https://doi.org/10.1021/acsenergylett.0c00109

[25] K. Zhu, Z. Sun, Z. Li, P. Liu, H. Li, L. Jiao, Design Strategies and Recent Advancements for Low-Temperature Aqueous Rechargeable Energy Storage,

Adv. Energy Mater. 13 (2023) 2203708. https://doi.org/10.1002/aenm.202203708

[26] J. Hao, L. Yuan, C. Ye, D. Chao, K. Davey, Z. Guo, S. Z. Qiao, Boosting Zinc Electrode Reversibility in Aqueous Electrolytes by Using Low-Cost Antisolvents, Angew. Chem., Int. Ed. 60 (2021) 7366-7375. https://doi.org/10.1002/anie.202016531

[27] J. Liu, C. Yang, X. Chi, B. Wen, W. Wang, Y. Liu, Water/Sulfolane Hybrid Electrolyte Achieves Ultralow-Temperature Operation for High-Voltage Aqueous Lithium-Ion Batteries, Adv. Funct. Mater. 32 (2022) 2106811. https://doi.org/10.1002/adfm.202106811

[28] Q. Dou, S. Lei, D. Wang, Q. Zhang, D. Xiao, H. Guo, A. Wang, H. Yang, Y. Li, S. Shi, X. Yan, Safe and high-rate supercapacitors based on an "acetonitrile/water in salt" hybrid electrolyte, Energy Environ. Sci. 11 (2018) 3212-3219. https://doi.org/10.1039/c8ee01040d

[29] J. Chen, J. Vatamanu, L. Xing, O. Borodin, H. Chen, X. Guan, X. Liu, K. Xu, W. Li, Improving Electrochemical Stability and Low-Temperature Performance with Water/Acetonitrile Hybrid Electrolytes, Adv. Energy Mater. 10 (2020) 1902654. https://doi.org/10.1002/aenm.201902654

[30] N. Chang, T. Li, R. Li, S. Wang, Y. Yin, H. Zhang, X. Li, An aqueous hybrid electrolyte for low-temperature zinc-based energy storage devices, Energy Environ. Sci. 13 (2020) 3527-3535. https://doi.org/10.1039/d0ee01538e

[31] Y. Zhang, J. Xu, Z. Li, Y. Wang, S. Wang, X. Dong, Y. Wang, All-climate aqueous Na-ion batteries using "water-in-salt" electrolyte, Sci. Bull. 67 (2022) 161-170. https://doi.org/10.1016/j.scib.2021.08.010

[32] W. Sun, Z. Xu, C. Qiao, B. Lv, L. Gai, X. Ji, H. Jiang, L. Liu, Antifreezing Proton Zwitterionic Hydrogel Electrolyte via Ionic Hopping and Grotthuss Transport Mechanism toward Solid Supercapacitor Working at -50 °C, Adv. Sci. 9 (2022) 2201679. https://doi.org/10.1002/advs.202201679

[33] J. Xu, J. Zhang, T. P. Pollard, Q. Li, S. Tan, S. Hou, H. Wan, F. Chen, H. He, E. Hu, K. Xu, X. Q. Yang, O. Borodin, C. Wang, Electrolyte design for Li-ion batteries under extreme operating conditions, Nature 614 (2023) 694-700. https://doi.org/10.1038/s41586-022-05627-8

[34] Q. Wang, C. Zhao, Z. Yao, J. Wang, F. Wu, S. G. H. Kumar, S. Ganapathy, S. Eustace, X. Bai, B. Li, J. Lu, M. Wagemaker, Entropy-Driven Liquid Electrolytes for Lithium Batteries, Adv. Mater. 35 (2023) 2210677. https://doi.org/10.1002/adma.202210677

[35] Y. Qian, Y. Chu, Z. Zheng, Z. Shadike, B. Han, S. Xiang, Y. Kang, S. Hu, C. Cao, L. Zhong, Q. Shi, M. Lin, H. Zeng, J. Wang, E. Hu, C. Weiland, X. Q. Yang, Y. Deng, A new cyclic carbonate enables high power/low temperature lithium-ion batteries, Energy Storage Mater. 45 (2022) 14-23. https://doi.org/10.1016/j.ensm.2021.11.029

[36] M. Wang, T. Li, Y. Yin, J. Yan, H. Zhang, X. Li, A -60 °C Low-Temperature Aqueous Lithium Ion-Bromine Battery with High Power Density Enabled by

Electrolyte Design, Adv. Energy Mater. 12 (2022) 2200728. https://doi.org/10.1002/aenm.202200728

[37] Z. Wang, H. Zhang, J. Xu, A. Pan, F. Zhang, L. Wang, R. Han, J. Hu, M. Liu, X. Wu, Advanced Ultralow-Concentration Electrolyte for Wide-Temperature and High-Voltage Li-Metal Batteries, Adv. Funct. Mater. 32 (2022) 2112598. https://doi.org/10.1002/adfm.202112598

[38] Y. Sun, H. Ma, X. Zhang, B. Liu, L. Liu, X. Zhang, J. Feng, Q. Zhang, Y. Ding, B. Yang, L. Qu, X. Yan, Salty Ice Electrolyte with Superior Ionic Conductivity Towards Low-Temperature Aqueous Zinc Ion Hybrid Capacitors, Adv. Funct. Mater. 31 (2021) 2101277. https://doi.org/10.1002/adfm.202101277

[39] D. J. Yoo, Q. Liu, O. Cohen, M. Kim, K. A. Persson, Z. Zhang, Rational Design of Fluorinated Electrolytes for Low Temperature Lithium-Ion Batteries, Adv. Energy Mater. 13 (2023) 2204182. https://doi.org/10.1002/aenm.202204182

[40] W. Deng, Z. Zhou, Y. Li, M. Zhang, X. Yuan, J. Hu, Z. Li, C. Li, R. Li, High-Capacity Layered Magnesium Vanadate with Concentrated Gel Electrolyte toward High-Performance and Wide-Temperature Zinc-Ion Battery, ACS Nano 14 (2020) 15776-15785. https://doi.org/10.1021/acsnano.0c06834

[41] M. Qiu, P. Sun, K. Han, Z. Pang, J. Du, J. Li, J. Chen, Z. Wang, W. Mai, Tailoring water structure with high-tetrahedral-entropy for antifreezing electrolytes and energy storage at -80 °C, Nat. Commun. 14 (2023) 601. https://doi.org/10.1038/s41467-023-36198-5

[42] F. Yue, Z. Tie, S. Deng, S. Wang, M. Yang, Z. Niu, An Ultralow Temperature Aqueous Battery with Proton Chemistry, Angew. Chem., Int. Ed. 60 (2021) 13882-13886. https://doi.org/10.1002/anie.202103722

[43] Y. Shi, R. Wang, S. Bi, M. Yang, L. Liu, Z. Niu, An Anti-Freezing Hydrogel Electrolyte for Flexible Zinc-Ion Batteries Operating at -70 °C, Adv. Funct. Mater. 33 (2023) 2214546. https://doi.org/10.1002/adfm.202214546

[44] T. Sun, X. Yuan, K. Wang, S. Zheng, J. Shi, Q. Zhang, W. Cai, J. Liang, Z. Tao, An ultralow-temperature aqueous zinc-ion battery, J. Mater. Chem. A 9 (2021) 7042-7047. https://doi.org/10.1039/d0ta12409e

[45] D. Feng, F. Cao, L. Hou, T. Li, Y. Jiao, P. Wu, Immunizing Aqueous Zn Batteries against Dendrite Formation and Side Reactions at Various Temperatures via Electrolyte Additives, Small 17 (2021) 2103195. https://doi.org/10.1002/smll.202103195

[46] E-Z. M. Ebeid, M. B. Zakaria, Temperature-modulated DSC (TMDSC), in: A. E-Z. Ebeid (Eds.), Thermal Analysis: From Introductory Fundamentals to Advanced Applications, Elsevier Inc., Amsterdam, 2021, pp. 41-128

[47] E. Parodi, L.E. Govaert, G.W.M. Peters, Glass transition temperature versus structure of polyamide 6: A flash-DSC study, Thermochimica Acta 657 (2017) 110-122. https://doi.org/10.1016/j.tca.2017.09.021

[48] R. He, T. Kyu, Effect of Plasticization on Ionic Conductivity Enhancement in Relation to Glass Transition Temperature of Crosslinked Polymer Electrolyte

Membranes, Macromolecules 49 (2016) 5637-5648. https://doi.org/10.1021/acs.macromol.6b00918

[49] Q. Dou, Y. Lu, L. Su, X. Zhang, S. Lei, X. Bu, L. Liu, D. Xiao, J. Chen, S. Shi, X. Yan, A sodium perchlorate-based hybrid electrolyte with high salt-to-water molar ratio for safe 2.5 V carbon-based supercapacitor, Energy Storage Mater. 23 (2019) 603-609. https://doi.org/10.1016/j.ensm.2019.03.016

[50] H. Bi, X. Wang, H. Liu, Y. He, W. Wang, W. Deng, X. Ma, Y. Wang, W. Rao, Y. Chai, H. Ma, R. Li, J. Chen, Y. Wang, M. Xue, A Universal Approach to Aqueous Energy Storage via Ultralow-Cost Electrolyte with Super-Concentrated Sugar as Hydrogen-Bond-Regulated Solute, Adv. Mater. 32 (2020) 2000074. https://doi.org/10.1002/adma.202000074

[51] J. H. Park, Y. J. Oh, D. Y. Park, J. Lee, J. S. Park, C. R. Park, J. H. Kim, T. Kim, S. J. Yang, A New Class of Carbon Nanostructures for High-Performance Electro-Magnetic and -Chemical Barriers, Adv. Sci. 8 (2021) 2102718. https://doi.org/10.1002/advs.202102718

[52] H. I. Kim, E. Shin, S. H. Kim, K. M. Lee, J. Park, S. J. Kang, S. So, K. C. Roh, S. K. Kwak, S. Y. Lee, Aqueous eutectic lithium-ion electrolytes for wide-temperature operation, Energy Storage Mater. 36 (2021) 222-228. https://doi.org/10.1016/j.ensm.2020.12.024

[53] Y. Hu, R. Shi, Y. Ren, W. Peng, C. Feng, Y. Zhao, S. Zheng, W. Li, Z. Sun, J. Guo, S. Guo, X. Wang, F. Yan, A "Two-in-One" Strategy for Flexible Aqueous

Batteries Operated at -80 °C, Adv. Funct. Mater. 32 (2022) 2203081. https://doi.org/10.1002/adfm.202203081

[54] Q. Zhang, K. Xia, Y. Ma, Y. Lu, L. Li, J. Liang, S. Chou, J. Chen, Chaotropic Anion and Fast-Kinetics Cathode Enabling Low-Temperature Aqueous Zn Batteries, ACS Energy Lett. 6 (2021) 2704-2712. https://doi.org/10.1021/acsenergylett.1c01054

[55] Q. Nian, S. Liu, J. Liu, Q. Zhang, J. Shi, C. Liu, R. Wang, Z. Tao, J. Chen, All-Climate Aqueous Dual-Ion Hybrid Battery with Ultrahigh Rate and Ultralong Life Performance, ACS Appl. Energy Mater. 2 (2019) 4370-4378. https://doi.org/10.1021/acsaem.9b00566

[56] J. Li, S. Tang, J. Hao, Q. Yuan, T. Wang, L. Pan, J. Li, S. Yang, C. Wang, Interfacial built-in electric field and crosslinking pathways enabling $WS_2/Ti_3C_2T_X$ heterojunction with robust sodium storage at low temperature, J. Energy Chem. 89 (2024) 635-645. https://doi.org/10.1016/j.jechem.2023.10.037

[57] L. Tao, P. Sittisomwong, B. Ma, A. Hu, D. Xia, S. Hwang, H. Huang, P. Bai, F. Lin, Tailoring solid-electrolyte interphase and solvation structure for subzero temperature, fast-charging, and long-cycle-life sodium-ion batteries, Energy Storage Materials 55 (2023) 826-835. https://doi.org/10.1016/j.ensm.2022.12.042

[58] L. Deng, K. Goh, F. D. Yu, Y. Xia, Y. S. Jiang, W. Ke, Y. Han, L. F. Que, J. Zhou, Z. B. Wang, Self-optimizing weak solvation effects achieving faster low-

temperature charge transfer kinetics for high-voltage $Na_3V_2(PO_4)_2F_3$ cathode, Energy Storage Materials 44 (2022) 82-92. https://doi.org/10.1016/j.ensm.2021.10.012